1. Extended Data

Figure #	Figure title One sentence only	Filename This should be the name the file is saved as when it is uploaded to our system. Please include the file extension. i.e.: *Smith_ED_Fi_1.jpg*	Figure Legend If you are citing a reference for the first time in these legends, please include all new references in the Online Methods References section, and carry on the numbering from the main References section of the paper.
Extended Data Fig. 1			
Extended Data Fig. 2			
Extended Data Fig. 3			
Extended Data Fig. 4			
Extended Data Fig. 5			
Extended Data Fig. 6			
Extended Data Fig. 7			
Extended Data Fig. 8			
Extended Data Fig. 9			
Extended Data Fig. 10			

2. Supplementary Information:

A. Flat Files

Item	Present?	Filename This should be the name the file is saved as when it is uploaded to our system, and should include the file extension. The extension must	A brief, numerical description of file contents. i.e.: *Supplementary Figures 1-4, Supplementary Discussion, and Supplementary Tables 1-4.*

		be .pdf	
Supplementary Information	Yes	Supplementary_ Information.pdf	Supplementary Table 1, and Supplementary Figures 1-19.
Reporting Summary	No		

B. Additional Supplementary Files

Type	Number If there are multiple files of the same type this should be the numerical indicator. i.e. "1" for Video 1, "2" for Video 2, etc.	Filename This should be the name the file is saved as when it is uploaded to our system, and should include the file extension. i.e.: *Smith_ Supplementary_Video_1.mov*	Legend or Descriptive Caption Describe the contents of the file
Choose an item.			
Choose an item.			
Choose an item.			
Choose an item.			
Choose an item.			
Choose an item.			

3. Source Data

Parent Figure or Table	Filename This should be the name the file is saved as when it is uploaded to our system, and should include the file extension. i.e.: *Smith_SourceData_Fig1.xls,* or *Smith_ Unmodified_Gels_Fig1.pdf*	Data description e.g.: Unprocessed Western Blots and/or gels, Statistical Source Data, etc.
Source Data Fig. 1		
Source Data Fig. 2		
Source Data Fig. 3		
Source Data Fig. 4		
Source Data Fig. 5		
Source Data Fig. 6		
Source Data		

Fig. 7		
Source Data Fig. 8		
Source Data Extended Data Fig. 1		
Source Data Extended Data Fig. 2		
Source Data Extended Data Fig. 3		
Source Data Extended Data Fig. 4		
Source Data Extended Data Fig. 5		
Source Data Extended Data Fig. 6		
Source Data Extended Data Fig. 7		
Source Data Extended Data Fig. 8		
Source Data Extended Data Fig. 9		
Source Data Extended Data Fig. 10		

Amplified Madden-Julian oscillation impacts in Pacific-North America region

Wenyu Zhou[1*], Da Yang[1,2], Shang-Ping Xie[3] and Jing Ma[4]

[1]Lawrence Berkeley National Laboratory, Berkeley, California, USA

[2]University of California Davis, Davis, California, USA

[3]University of California San Diego, La Jolla, California, USA

[4]Collaborative Innovation Center on Forecast and Evaluation of Meteorological Disasters/KLME/ILCEC, Nanjing University of Information Science and Technology, Nanjing, China

*Corresponding Author: wenyuzhou@lbl.gov

Abstract

The Madden-Julian Oscillation (MJO) is a slow-moving tropical mode that produces a planetary-scale envelope of convective storms. By exciting Rossby waves, it creates teleconnections with far-reaching impacts on extratropical circulation and weather. While recent studies have investigated the MJO's response to anthropogenic warming, not much is known about potential changes in its teleconnections. Here we show that the MJO

teleconnection pattern in boreal winter will likely extend further eastward over the North Pacific. This is due primarily to an eastward shift in the exit region of the subtropical jet, on which the teleconnection pattern is anchored, and additionally contributed by an eastward extension of the MJO itself. The eastward-extended teleconnection allows the MJO to exert a greater impact downstream on the Northeast Pacific and North American west coast. Over California specifically, the multi-model mean projects a ~54% increase in MJO-induced precipitation variability by 2100 under a high emissions scenario.

Main

The MJO[1,2] is distinct from typical equatorial waves because of its planetary spatial scale and slow eastward propagation. The anomalous circulation and cloudiness span a horizontal scale of ~10,000 km and travel over the tropical Indian and West Pacific oceans at a speed of ~5 m s^{-1}. It usually takes more than 20 days for the large-scale convection to alternate between enhanced and suppressed states. This allows the tropical MJO to excite quasi-stationary Rossby waves that propagate into the extratropics[3–5] and exert far-reaching impacts on regional circulation and weather[6]. The MJO teleconnection is known to affect prominent climate features including the Pacific-North America (PNA) Pattern[7,8], North Atlantic Oscillation[9,10], stratospheric sudden warming[11,12], hurricanes[13] and monsoons[14]. Its effect on the PNA pattern, in particular, modulates blocking[15] and atmospheric rivers[16] in the Northeast Pacific, leading to profound regional impacts along the west coast of North America. The MJO is an important predictor for extended forecast beyond two weeks[17].

The MJO involves intricate interplays among wave dynamics, moist convection, radiation and

air-sea coupling. Extensive studies have been devoted to investigating its physics[18–22] and numerical simulation[23–26]. The overall representation of the MJO in global climate models (GCMs) is appreciably improved in the Coupled Model Intercomparison Project Phase 5 (CMIP5)[25] and the new CMIP6. Using selected models that properly simulate the MJO, recent studies have started to investigate future changes of the MJO[27–29]. It is found that, while the MJO precipitation and associated convective heating will increase with enhanced vertical moisture gradient, its dynamic amplitude as measured by either surface wind or pressure velocity may decrease due to enhanced dry static stability and more top-heavy profile of convection[30–32].

The impacts of the MJO on the extratropics depend on its teleconnection pattern, whose responses to anthropogenic warming are however largely unexplored. It is suspected that a weakened MJO dynamic amplitude may lead to a weakened teleconnection pattern[32], as seen in one specific model[33], but a systematic investigation is still lacking. Here, based on multiple models that properly simulate the MJO, we show that future changes of the MJO teleconnection mainly manifest an eastward-extended pattern while changes in the amplitude are uncertain. The eastward-extended teleconnection is driven by theoretically-predicted large-scale changes and can be reproduced in a simple linear model. This allows the MJO to produce a larger subseasonal variability in the downstream regions, which may upset societal sectors such as agriculture, flood control and resource management.

Amplified MJO impacts from eastward-extended teleconnection

The response of the MJO teleconnection to anthropogenic warming is investigated in eleven GCMs (Supplementary Table 1), which are selected from the CMIP5 and CMIP6 archives

according to their ability to properly simulate the MJO[25,34] (Methods; Supplementary Fig. 1). The present and future warmer climates are represented by the historical (HIST) and Representative Concentration Pathway 8.5 (RCP8.5) experiments, respectively. We focus on the boreal winter (December to March) when the MJO teleconnection in the Northern Hemisphere is most significant and the west coast of North America is in its rainy season. To extract the MJO-induced signals, the daily anomalous fields are band-passed (20-100 day) and composited according to the MJO phase (Methods). The tropical state, indicated by the anomalous 500-hPa pressure velocity (ω_{500}), is composited concurrently; while the extratropical teleconnection pattern, indicated by the anomalous 250-hPa geopotential height (Z_{250}), ω_{500} and precipitation, is composited at a 6-day lag. In Phase 3, the tropical MJO circulation centers around the Maritime Continent and a classic PNA teleconnection pattern[35] emerges in the extratropics (Fig. 1a). The MJO-PNA pattern features strong Z_{250} signals near the subtropical jet exit[7,36,37] (where the westerly decelerates, $\partial\overline{U}/\partial x < 0$), as a result of barotropic energy conversion which allows waves to effectively extract energy from the zonally asymmetric climatology[7,38,39]. The positive Z_{250} anomaly over the Northeast Pacific is associated with large-scale subsidence and drying near the west coast of North America. An opposite teleconnection pattern is found in Phase 7 (Supplementary Fig. 2). In Phase 1 and 5, the Rossby-wave trains are emitted from the Indian ocean and weakly affect the Northeast Pacific (Supplementary Fig. 2). Throughout the eight phases, the MJO teleconnection induces substantial Z_{250} variability that peaks near the jet exit (Fig. 1b). The associated ω_{500} and precipitation variability are most significant around 30^{o}N and along the west coast of North America. The simulated MJO teleconnection is compared against those constructed from two reanalysis datasets (Supplementary Fig. 3). The overall patterns are similar but the simulated pattern appears to be weaker and more eastward. The eastward bias is

113 likely related to an eastward bias in the jet exit in GCMs (Fig. 1a and Supplementary Fig. 3a).

114

115 We show that the MJO-PNA teleconnection pattern will extend further eastward under
116 anthropogenic warming, as indicated by eastward shifts in both the center and eastern flank of
117 Z_{250} (Fig. 1a,c). The eastward-extended teleconnection leads to a deeper intrusion and
118 intensification of subsidence and drying (or ascent and wetting in Phase 7) near the west coast of
119 North America (Fig. 1a,c; Supplementary Fig. 2). A consistent eastward extension is found in
120 Phase 1 and 5 (Supplementary Fig. 2). As a result, the MJO-induced variability (measured by the
121 standard deviation across the phases) extends further eastward, with amplified variation in Z_{250}
122 over the Northeast Pacific and in ω_{500} and precipitation along the west coast of North America
123 (Fig. 1b,d). Zooming into the precipitation response, the Hovmöller diagram averaged over
124 $30^{o}\mathrm{N}-40^{o}\mathrm{N}$ clearly illustrates that the MJO extratropical impacts extend further eastward,
125 driving a larger precipitation variability over the downstream regions (Fig. 1e). Over California
126 specifically, the MJO-induced precipitation variability is amplified by more than 50%, with the
127 interphase standard deviation increasing from 0.3 mm d^{-1} to 0.47 mm d^{-1} (Fig. 1f). It is also
128 hinted that the eastward-extended teleconnection allows the MJO impacts to arrive earlier in
129 phase in California (indicated by the yellow line in Fig. 1e), leading to a forward shift in the
130 MJO-phase-composited impacts (Fig. 1f).

131

132 Unlike the notable eastward extension, the amplitude change of the MJO teleconnection is subtle
133 in the multi-model mean, as measured by either the phase-composited Z_{250} peak value (Fig. 1a,c)
134 or Z_{250} variability (Fig. 1b,d). As we will discuss later, there is large uncertainty in the
135 teleconnection amplitude change among models.

Causes of the eastward-extended MJO teleconnection

In light of the profound impacts of the eastward-extended MJO teleconnection, it is important to understand its causes. The MJO teleconnection pattern depends on both the tropical MJO forcing and the extratropical large-scale mean state, which modulate the source and propagation of the Rossby-wave train, respectively[34,40–42]. Under anthropogenic warming, notable changes are projected in both factors. In the tropics, the MJO-phase-composited ω_{500} extends further eastward into the central Pacific (Fig. 1a,c). Both the centroid and boundary of the MJO ω_{500} variability move eastward (Fig. 1b,d). This eastward extension of the MJO itself has been noticed in previous studies[32,43,44] and may drive a corresponding change in the extratropical teleconnection. In the extratropics, the subtropical jet exit is projected to shift eastward[45] (purple contours from Fig. 1a to Fig. 1c). The MJO teleconnection pattern, which is anchored on the jet exit through the barotropic energy conversion, may extend eastward correspondingly.

To test these hypotheses and examine their relative importance, we turn to a simple linear baroclinic model (LBM) that simulates linear responses to an eastward-propagating MJO heating in the presence of a prescribed large-scale mean state (Methods). With imposed MJO heating and mean state diagnosed from the HIST simulations of GCMs, LBM reasonably captures the tropical MJO circulation and its extratropical teleconnection pattern (Fig. 2a). The Z_{250} responses peak near the jet exit region, similar to those in reanalysis and comprehensive GCMs. Under anthropogenic warming, the MJO heating extends eastward and increases, while the mean state changes feature an eastward shift of the jet exit and a larger dry static stability (Supplementary Fig. 4). When both the MJO heating and mean state are changed to those in

RCP8.5 (Fig. 2b), the teleconnection pattern extends eastward by 8^{o} (measured by shift in the Z_{250} center) and weakens slightly. The effect of the eastward extension dominates and leads to an amplified large-scale descent near the west coast of North America. Simulations with changing mean state (Fig. 2c) or MJO heating (Fig. 2d) only are conducted to further decompose the causes. It is found that the eastward-extended teleconnection is mainly driven by the jet-exit shift, which leads to a 6^{o} teleconnection shift (Fig. 2c), and additionally contributed by the eastward-extended MJO heating, which leads to a smaller 2^{o} shift (Fig. 2d). The slightly-weakened teleconnection amplitude reflects a net result of the opposing effects of the larger static stability (Fig. 2c) and the stronger MJO heating (Fig. 2d). Considering the bias of the climatological jet in the multi-model mean of GCMs, we have conducted additional LBM simulations for models with a good representation of the climatological jet. It is confirmed that the MJO teleconnection extends eastward as long as the jet exit shifts eastward (Supplementary Fig. 5).

Drivers of MJO extension and jet-exit shift

What then drives the eastward extension of the MJO itself and the eastward shift of the subtropical jet exit? The distribution of the MJO activity is known to be sensitive to the tropical warming pattern[46]. Here we provide further evidence that the zonally asymmetric warming along the Equator drives the eastward extension of the MJO. To illustrate this point, AMIP (Atmospheric Model Intercomparison Project)-style simulations forced with uniform warming (AMIP4K) and projected patterned warming (AMIPFuture) are utilized (Methods). Although these AMIP-style experiments do not consider the atmosphere-ocean coupling, their MJO propagation characteristics are similar to those of coupled models, as shown by the Hovmöller

diagram of the equatorial-mean ω_{500} (Fig. 3a-c). We find that the eastward MJO extension projected in coupled models (Fig. 3a) is absent in AMIP4K with uniform warming (Fig. 3b) and only reproduced in AMIPFuture with patterned warming (Fig. 3c). The projected warming pattern features enhanced warming east of the climatological warm pool (Fig. 3d), which works to extend the convectively-unstable/moist region and thus the MJO activity eastward (Supplementary Fig. 6). The critical role of the zonally asymmetric warming can be further seen from the intermodel spread of coupled models. Under anthropogenic warming, the more the Central Pacific is warmed compared to the West Pacific, the more the MJO extends eastward (Fig. 3e).

The exit of the subtropical jet is integrally tied to the stationary eddy pattern, which is defined as the departure in the 250-hPa geopotential height from the zonal mean (Z^*_{250}). With the strongest (weakest) jet lying south of the anomalous low (high), the jet exits near the node of Z^*_{250} (Fig. 4a). Under anthropogenic warming, the stationary eddy pattern is known to shift eastward in boreal winter[47], leading to a corresponding shift in the jet exit (Fig. 4b). Among models, the shift of the jet exit (measured by the outer contour of the subtropical jet) is highly correlated with that of the Z^*_{250} node (Supplementary Fig. 7a). The eastward shift of Z^*_{250} has been attributed to an increase in the stationary Rossby wavelength due to the strengthened westerlies[47] (the stationary wavelength L in linear barotropic theory[3] scales with the jet speed U as $L \sim \sqrt{U/\beta^*}$ where $\beta^* = \beta - U_{yy}$ is the meridional gradient of the absolute vorticity). The strengthened westerlies are in turn driven by the increased meridional temperature gradient due to enhanced warming in the tropical upper-troposphere (Fig. 4c). This enhanced tropical upper-tropospheric warming is a direct consequence of the moist-adiabat adjustment and exists even in the AMIP-style simulation

forced with uniform warming (Fig. 4c). Thus, eastward shifts of Z^*_{250} and the jet exit are consistently found from AMIP to AMIP4K (Fig. 4b), leading to a robust eastward extension of the MJO teleconnection under uniform warming (Fig. 4d).

The subtropical jet may also respond to rectification effects of the MJO changes[48] or zonal shift in the Walker circulation. However, it is unlikely that these factors play a significant role in driving the projected jet-exit shift. We note that the eastward jet-exit shift is robustly projected in models that predict opposite changes in the MJO pattern (either eastward or slightly westward, Supplementary Fig. 7b) and amplitude (either positive or negative, Supplementary Fig. 7c). The magnitude of the jet-exit shift in AMIP4K is similar to that in AMIPFuture (Fig. 4b), even though the Walker-circulation shift is only projected under patterned warming (Supplementary Fig. 8). Despite little difference in the jet-exit shift, the eastward extension of the MJO teleconnection is more pronounced in AMIPFuture than in AMIP4K (Fig. 4d). This is likely due to the contribution from the eastward extension of the MJO under patterned warming (Fig. 3c).

Robust eastward extension and uncertain amplitude change

The results above are mainly based on the multi-model mean. We now look into results of individual models (Supplementary Figs. 9-19) and illustrate the robustness in the eastward extension of the MJO teleconnection as well as the uncertainty in the teleconnection amplitude change. Across models, the eastward extension of the MJO teleconnection pattern (measured by the centroid of the MJO-induced Z_{250} variability) is significantly correlated with the shift of the subtropical jet exit (Fig. 5a). Nine out of the eleven selected models (21 out of the total 25 models including those not selected due to lack of good MJOs or outputs) predict an eastward

228 shift of the subtropical jet exit. In the multi-model mean, there is a ~7^{o} eastward shift in the jet
229 exit and a ~7.5^{o} eastward extension in the MJO teleconnection pattern. The eastward jet-exit shift
230 is insensitive to the climatological bias of a more eastward jet exit in GCMs. It is robustly
231 projected in models with both good and biased jet climatology and no correlation is found
232 between future shift and climatological position of the jet exit (Supplementary Fig. 7d). The
233 intermodel correlation between eastward extensions of the teleconnection pattern and the MJO
234 itself is found to be insignificant (Fig. 5b). This is consistent with the LBM results, which show
235 that changes in MJO heating are less effective in changing the teleconnection pattern than the jet-
236 exit shift.
237
238 Models with a more eastward-extended MJO teleconnection exhibit a larger amplification in the
239 MJO-induced variability in California (Fig. 5c). Nine out of the eleven models predict amplified
240 MJO impacts and the multi-model mean predicts a 35% (54%) increase in the MJO-induced
241 ω_{500} (precipitation) variability. The larger increase in precipitation variability, compared to that
242 in ω_{500}, may reflect the thermodynamic contribution from the enhanced atmospheric moisture
243 with warming. With the high correlation between the eastward-extend teleconnection and the jet-
244 exit shift (Fig. 5a), the amplification of the MJO impacts is further correlated with the jet-exit
245 shift (Fig. 5d). According to the intermodel linear regression (black and red lines), a one-degree
246 eastward shift of the jet exit implies a ~5% (6%) amplification in the MJO-induced ω_{500}
247 (precipitation) variability in California.
248
249 The MJO impacts would also be affected by changes in the amplitude of the MJO teleconnection.
250 However, models disagree with each other on whether the MJO teleconnection amplitude will be

weakened or amplified and the multi-model mean projects little change (Fig. 5e). The amplitude change of the MJO teleconnection is not simply correlated with that of tropical MJO circulation, indicating additional influences from extratropical dynamics. The teleconnection amplitude change does not play a major role in explaining the intermodel spread of the changing MJO impacts in California (Fig. 5f), which is largely dominated by that of the eastward extension (Fig. 5d).

Summary and discussion

In summary, our multi-GCM diagnosis and linear dynamic model experiments reveal an eastward extension of the MJO teleconnection to the Pacific-North America region in boreal winter under anthropogenic warming. This eastward extension is mainly due to the eastward shift of the subtropical jet exit, a large-scale climate response to the global-scale warming. Additionally, the equatorial warming pattern drives an eastward extension of tropical MJO convection and further enhances the teleconnection extension. The eastward-extended teleconnection allows the MJO to exert a larger impact in the Northeast Pacific and along the west coast of North America. Recent studies have warned increased interannual precipitation volatility in California under anthropogenic warming[49]. The enhanced subseasonal variability illustrated here will further aggravate the situation, posing acute challenges on regional resource management and extreme weather preparation. Similar to the subseasonal MJO-PNA teleconnection, the interannual ENSO (El Niño–Southern Oscillation)-forced PNA pattern is also projected to extend eastward under anthropogenic warming[50]. Such robust changes in the tropical-induced PNA teleconnection arise from zonal shifts in the large-scale mean state and imply increased predictability beyond week 2 over winter North America.

Compared to the notable eastward extension, the amplitude change of the MJO teleconnection is subtle in the multi-model mean and is uncertain among models. This uncertainty is not necessarily dominated by the tropical MJO forcing but can come from extratropical dynamics, such as changes in the dry static stability, zonal asymmetry of the large-scale flow and high-frequency eddy interaction. Future studies are needed to investigate the detailed mechanisms and constrain the uncertainty. Our work has focused on the Pacific-North America region which is located downstream of the eastward teleconnection extension and on the winter season when the MJO propagates more zonally. Further studies are needed to explore potential changes of the MJO impacts in other regions and seasons.

References

1. Madden, R. A. & Julian, P. R. Detection of a 40–50 Day Oscillation in the Zonal Wind in the Tropical Pacific. *J. Atmos. Sci.* **28**, 702–708 (1971).
2. Zhang, C. Madden-Julian Oscillation. *Reviews of Geophysics* **43**, (2005).
3. Hoskins, B. J. & Karoly, D. J. The Steady Linear Response of a Spherical Atmosphere to Thermal and Orographic Forcing. *J. Atmos. Sci.* **38**, 1179–1196 (1981).
4. Matthews, A. J., Hoskins, B. J. & Masutani, M. The global response to tropical heating in the Madden–Julian oscillation during the northern winter. *Quarterly Journal of the Royal Meteorological Society* **130**, 1991–2011 (2004).
5. Seo, K.-H. & Son, S.-W. The Global Atmospheric Circulation Response to Tropical Diabatic Heating Associated with the Madden–Julian Oscillation during Northern Winter. *J. Atmos. Sci.* **69**, 79–96 (2011).

6. Zhang, C. Madden–Julian Oscillation: Bridging Weather and Climate. *Bull. Amer. Meteor. Soc.* **94**, 1849–1870 (2013).
7. Mori, M. & Watanabe, M. The Growth and Triggering Mechanisms of the PNA: A MJO-PNA Coherence. *Journal of the Meteorological Society of Japan. Ser. II* **86**, 213–236 (2008).
8. Riddle, E. E. *et al.* The impact of the MJO on clusters of wintertime circulation anomalies over the North American region. *Clim Dyn* **40**, 1749–1766 (2013).
9. Cassou, C. Intraseasonal interaction between the Madden–Julian Oscillation and the North Atlantic Oscillation. *Nature* **455**, 523–527 (2008).
10. Lin, H., Brunet, G. & Derome, J. An Observed Connection between the North Atlantic Oscillation and the Madden–Julian Oscillation. *J. Climate* **22**, 364–380 (2009).
11. Garfinkel, C. I., Feldstein, S. B., Waugh, D. W., Yoo, C. & Lee, S. Observed connection between stratospheric sudden warmings and the Madden-Julian Oscillation. *Geophysical Research Letters* **39**, (2012).
12. Kang, W. & Tziperman, E. The MJO-SSW Teleconnection: Interaction Between MJO-Forced Waves and the Midlatitude Jet. *Geophysical Research Letters* **45**, 4400–4409 (2018).
13. Maloney, E. D. & Hartmann, D. L. Modulation of Eastern North Pacific Hurricanes by the Madden–Julian Oscillation. *J. Climate* **13**, 1451–1460 (2000).
14. Lorenz, D. J. & Hartmann, D. L. The Effect of the MJO on the North American Monsoon. *J. Climate* **19**, 333–343 (2006).
15. Henderson, S. A., Maloney, E. D. & Barnes, E. A. The Influence of the Madden–Julian Oscillation on Northern Hemisphere Winter Blocking. *J. Climate* **29**, 4597–4616 (2016).

16. Mundhenk, B. D., Barnes, E. A., Maloney, E. D. & Baggett, C. F. Skillful empirical subseasonal prediction of landfalling atmospheric river activity using the Madden–Julian oscillation and quasi-biennial oscillation. *npj Clim Atmos Sci* **1**, 1–7 (2018).
17. Johnson, N. C., Collins, D. C., Feldstein, S. B., L'Heureux, M. L. & Riddle, E. E. Skillful Wintertime North American Temperature Forecasts out to 4 Weeks Based on the State of ENSO and the MJO. *Wea. Forecasting* **29**, 23–38 (2013).
18. Raymond, D. J. & Fuchs, Ž. Moisture Modes and the Madden–Julian Oscillation. *J. Climate* **22**, 3031–3046 (2009).
19. Sobel, A. & Maloney, E. Moisture Modes and the Eastward Propagation of the MJO. *J. Atmos. Sci.* **70**, 187–192 (2012).
20. Yang, D. & Ingersoll, A. P. Triggered Convection, Gravity Waves, and the MJO: A Shallow-Water Model. *J. Atmos. Sci.* **70**, 2476–2486 (2013).
21. Adames, Á. F. & Kim, D. The MJO as a Dispersive, Convectively Coupled Moisture Wave: Theory and Observations. *J. Atmos. Sci.* **73**, 913–941 (2015).
22. Khairoutdinov, M. F. & Emanuel, K. Intraseasonal Variability in a Cloud-Permitting Near-Global Equatorial Aquaplanet Model. *J. Atmos. Sci.* **75**, 4337–4355 (2018).
23. Kim, D. *et al.* Application of MJO Simulation Diagnostics to Climate Models. *J. Climate* **22**, 6413–6436 (2009).
24. Jiang, X. *et al.* Vertical structure and physical processes of the Madden-Julian oscillation: Exploring key model physics in climate simulations. *Journal of Geophysical Research: Atmospheres* **120**, 4718–4748 (2015).
25. Ahn, M.-S. *et al.* MJO simulation in CMIP5 climate models: MJO skill metrics and process-oriented diagnosis. *Clim Dyn* **49**, 4023–4045 (2017).

26. Wang, B. *et al.* Dynamics-Oriented Diagnostics for the Madden–Julian Oscillation. *J. Climate* **31**, 3117–3135 (2018).
27. Liu, P. *et al.* MJO change with A1B global warming estimated by the 40-km ECHAM5. *Clim Dyn* **41**, 1009–1023 (2013).
28. Arnold, N. P., Branson, M., Kuang, Z., Randall, D. A. & Tziperman, E. MJO Intensification with Warming in the Superparameterized CESM. *J. Climate* **28**, 2706–2724 (2015).
29. Adames, Á. F., Kim, D., Sobel, A. H., Genio, A. D. & Wu, J. Changes in the structure and propagation of the MJO with increasing CO2. *Journal of Advances in Modeling Earth Systems* **9**, 1251–1268 (2017).
30. Bui, H. X. & Maloney, E. D. Changes in Madden-Julian Oscillation Precipitation and Wind Variance Under Global Warming. *Geophysical Research Letters* **45**, 7148–7155 (2018).
31. Bui, H. X. & Maloney, E. D. Mechanisms for Global Warming Impacts on Madden–Julian Oscillation Precipitation Amplitude. *J. Climate* **32**, 6961–6975 (2019).
32. Maloney, E. D., Adames, Á. F. & Bui, H. X. Madden–Julian oscillation changes under anthropogenic warming. *Nature Clim Change* **9**, 26–33 (2019).
33. Wolding, B. O., Maloney, E. D., Henderson, S. & Branson, M. Climate change and the Madden-Julian Oscillation: A vertically resolved weak temperature gradient analysis. *Journal of Advances in Modeling Earth Systems* **9**, 307–331 (2017).
34. Henderson, S. A., Maloney, E. D. & Son, S.-W. Madden–Julian Oscillation Pacific Teleconnections: The Impact of the Basic State and MJO Representation in General Circulation Models. *J. Climate* **30**, 4567–4587 (2017).
35. Wallace, J. M. & Gutzler, D. S. Teleconnections in the Geopotential Height Field during the Northern Hemisphere Winter. *Mon. Wea. Rev.* **109**, 784–812 (1981).

36. Bao, M. & Hartmann, D. L. The response to MJO-like forcing in a nonlinear shallow-water model. *Geophysical Research Letters* **41**, 1322–1328 (2014).

37. Adames, Á. F. & Wallace, J. M. Three-Dimensional Structure and Evolution of the MJO and Its Relation to the Mean Flow. *J. Atmos. Sci.* **71**, 2007–2026 (2014).

38. Simmons, A. J., Wallace, J. M. & Branstator, G. W. Barotropic Wave Propagation and Instability, and Atmospheric Teleconnection Patterns. *J. Atmos. Sci.* **40**, 1363–1392 (1983).

39. Ting, M. & Yu, L. Steady Response to Tropical Heating in Wavy Linear and Nonlinear Baroclinic Models. *J. Atmos. Sci.* **55**, 3565–3582 (1998).

40. Hoskins, B. J. & Ambrizzi, T. Rossby Wave Propagation on a Realistic Longitudinally Varying Flow. *J. Atmos. Sci.* **50**, 1661–1671 (1993).

41. Ting, M. & Sardeshmukh, P. D. Factors Determining the Extratropical Response to Equatorial Diabatic Heating Anomalies. *J. Atmos. Sci.* **50**, 907–918 (1993).

42. Yasui, S. & Watanabe, M. Forcing Processes of the Summertime Circumglobal Teleconnection Pattern in a Dry AGCM. *J. Climate* **23**, 2093–2114 (2009).

43. Subramanian, A. *et al.* The MJO and global warming: a study in CCSM4. *Clim Dyn* **42**, 2019–2031 (2014).

44. Chang, C.-W. J., Tseng, W.-L., Hsu, H.-H., Keenlyside, N. & Tsuang, B.-J. The Madden-Julian Oscillation in a warmer world. *Geophysical Research Letters* **42**, 6034–6042 (2015).

45. Neelin, J. D., Langenbrunner, B., Meyerson, J. E., Hall, A. & Berg, N. California Winter Precipitation Change under Global Warming in the Coupled Model Intercomparison Project Phase 5 Ensemble. *J. Climate* **26**, 6238–6256 (2013).

46. Maloney, E. D. & Xie, S.-P. Sensitivity of tropical intraseasonal variability to the pattern of climate warming. *Journal of Advances in Modeling Earth Systems* **5**, 32–47 (2013).

47. Simpson, I. R., Seager, R., Ting, M. & Shaw, T. A. Causes of change in Northern Hemisphere winter meridional winds and regional hydroclimate. *Nature Climate Change* **6**, 65–70 (2016).
48. Kang, W. & Tziperman, E. More Frequent Sudden Stratospheric Warming Events due to Enhanced MJO Forcing Expected in a Warmer Climate. *J. Climate* **30**, 8727–8743 (2017).
49. Swain, D. L., Langenbrunner, B., Neelin, J. D. & Hall, A. Increasing precipitation volatility in twenty-first-century California. *Nature Clim Change* **8**, 427–433 (2018).
50. Zhou, Z.-Q., Xie, S.-P., Zheng, X.-T., Liu, Q. & Wang, H. Global Warming–Induced Changes in El Niño Teleconnections over the North Pacific and North America. *J. Climate* **27**, 9050–9064 (2014).

Methods

CMIP outputs

The historical (HIST) and Representative Concentration Pathway 8.5 (RCP8.5 for CMIP5; SSP585 for CMIP6) experiments of eleven coupled GCMs are used to project changes in the MJO teleconnection under anthropogenic warming. The present and future climates are defined as HIST during 1979–2005 and RCP8.5 during 2079–2099, respectively. The eleven models are selected based on their ability to simulate reasonable MJO. In particular, Hovmöller diagrams of MJO-phase-composited equatorial precipitation are plotted for each model, as in Fig. 4 of ref. 25 (also see Supplementary Figs. 9-19.k for our computations that include CMIP6 models). Models that simulate reasonable MJO propagation in general have good values in the metric "the precipitation East-West Power Ratio", which is computed by the Program for Climate Model Diagnosis & Intercomparison (PCMDI) and available online at https://pcmdi.llnl.gov/pmp-

preliminary-results/mjo_metrics/mjo_ewr_cmip5and6_overlap_runs_average_standalone.html. The selected models, denoted with triangle symbols in the metric plot (Supplementary Fig. 1), are summarized in Supplementary Table 1 with their names, resolutions and model centers. Eight of them are from CMIP5[51]. They are CMCC-CM (1), CNRM-CM5 (2), IPSL-CM5B-LR (3), MIROC5 (4), MPI-ESM-LR (5), MRI-CGCM3 (6), NorESM1-M (7) and bcc-csm1-1 (8). Three of them are from the new CMIP6[52] (only a few models are available now with daily outputs). They are BCC-CSM2-MR (9), GFDL-CM4 (10) and MRI-ESM2 (11). Indexes in the parentheses are used for denoting individual models in the scatterplots. The CESM2 and CNRM-CM6 also simulate reasonable East-West Power Ratio in their HIST simulations but both of them at this time lack daily outputs of required variables for investigating future projection.

Among these eleven coupled models, six of them provide a complete set of AMIP, AMIP4K and AMIPFuture experiments, which are used to investigate the effects of global-scale and patterned warming on the eastward shift of the jet exit and on the eastward extension of the MJO. The six models are bcc-csm1-1, CNRM-CM5, MIROC5, MRI-CGCM3, BCC-CSM2-MR and MRI-ESM2. The AMIP simulation is forced with the observed SST. In AMIP4K, a globally uniform warming of 4 K is superimposed on the observed SST. AMIPFuture instead uses a spatially-patterned warming derived from the CMIP3 1pctCO2 simulation (averaged around the time when CO2 is quadrupled). This warming pattern is similar to those projected in RCP8.5.

The daily-mean data is used for MJO-related diagnosis and the monthly-mean data is used for analyzing the large-scale mean-state changes. For Fig. 5a and Supplementary Fig. 7, we have included fourteen extra models to investigate the robustness of the eastward shift in the jet exit.

They are ACCESS1-0, ACCESS1-3, BNU-ESM, CCSM4, CanESM2, CESM1-CAM5, GFDL-CM3, GISS-E2-R, HadGEM2-ES, IPSL-CM5A-LR, MIROC-ESM, inmcm4, CESM2 and CNRM-CM6. All model outputs have been interpolated to a common grid of 1.5° (lat) × 2.5° (lon) resolution before analysis. Metrics such as longitudes of the jet exit and Z^*_{250} node are computed after further interpolating to a finer resolution of 0.2^o.

Reanalysis Datasets:

MJO and its teleconnection are also constructed from two reanalysis datasets: NCEP-DOE[53] and ECMWF-ERA5[54]. Daily outputs including zonal winds, pressure velocity, geopotential height and precipitation are used. The analysis is for boreal winter (December to March) and covers the same HIST period (1979-2005).

Linear Baroclinic Model

We use a linear baroclinic model (LBM[55,56]) to explain the GCM-projected eastward extension of the MJO teleconnection. LBM has been widely used in previous studies of the MJO teleconnection[33,34,57,58]. In LBM, the hydrostatic primitive equations are linearized about a mean state and the linear response to a prescribed forcing is simulated. The resolution is set to T42L20, that is, 128 × 64 grids in the horizontal and 20 sigma levels in the vertical. Horizontal diffusion with an e-folding time scale of 2 h is applied. The model also applies Newtonian damping with a time scale of 20 days for most vertical levels and a time scale of 0.5 days for the lowest and highest levels.

The model is forced by a time-evolving, eastward-propagating MJO heating (Q). We constructed

this Q from the MJO-phase-composited 500-Pa pressure velocity ($\omega_{500}{}^{n}$) in GCMs according to the first-order dry static energy (s) balance, that is,

$$Q \cong \omega \frac{\partial s}{\partial p}.$$

First, the MJO-phase-composited heating (Q^n) is estimated from $\omega_{500}{}^{n}$ at each grid point (x, y) as,

$$Q^n(x, y, \eta) = \frac{\partial s}{\partial p} \cdot \omega_{500}{}^{n}(x, y) \cdot \cos^2(\eta - 0.5)\pi$$

where n refers to the MJO phase and η is the vertical sigma level. The tropical dry static stability $\frac{\partial s}{\partial p}$ is estimated from the boreal-winter climatology over the tropical Indian and West Pacific Oceans. It is 0.06 K hPa^{-1} for HIST and 0.075 K hPa^{-1} around the level of 500 hPa (Supplementary Fig. 4). Second, an eastward-propagating MJO heating is constructed by interpolating Q^n at eight phases to an assumed 48-days life cycle of MJO, with 6 days for each phase. The large-scale mean state, which includes winds, temperature, geopotential height and surface pressure, is constructed from the boreal-winter climatology in GCMs. The independent effect of MJO heating and mean state is then examined by changing them from that in HIST to that in RCP8.5.

MJO-related diagnostics

The MJO life cycle is categorized into eight MJO phases, which correspond to different longitudinal locations of the enhanced convection. Following the MJO Diagnostics Package[59] provided by the U.S. Climate Variability and Predictability (CLIVAR) MJO Working Group, we compute the MJO-phase-composited fields in the following five steps: 1) Subseasonal (20–100 day) bandpass-filtered anomalies are constructed by applying a 201-point Lanczos filter to

unfiltered anomalies from the climatological daily mean. 2) The first two leading empirical orthogonal functions (EOFs) of the MJO meridional pattern are generated using the equatorial-mean (10°N–10°S) subseasonal anomalies of 850-hPa zonal winds, 200-hPa zonal winds, and outgoing longwave radiation (OLR). OLR is derived from NOAA satellite data and zonal winds are from the NCEP–DOE reanalysis. 3) The real-time multivariable MJO (RMM^{60}) indices are computed for each selected model by projecting the simulated anomalous OLR and 250- and 850-hPa zonal winds onto the reanalysis EOFs. Projection onto the reanalysis EOFs allows for a consistent framework for comparison among different models. 4) The MJO phase is determined by $\tan^{-1}$(RMM2/RMM1), with each phase spanning 45^{o} of the cycle. Phase 3 corresponds to enhanced convection over the tropical East Indian and Phase 7 is characterized by enhanced convection over the tropical West Pacific. 5) Days associated with an active MJO phase are identified when the MJO amplitude ($\sqrt{\mathrm{RMM1}^2 + \mathrm{RMM2}^2}$) is greater than 1. Both concurrent and lag composites are obtained. The concurrent composite takes the mean of all the days at a particular MJO phase while the X-day lag composite collects all the days that are X-day lag of a particular MJO phase. Some of the analysis codes are adapted from the NCL scripts, available at https://www.ncl.ucar.edu/Applications/mjoclivar.shtml.

Following ref. 34, a two-tailed Student's t-test is used to identify where the MJO-phase-composited anomaly is significantly different from zero. The degree of freedom is set for each phase as N/dM (~80), where N represents the total number of days per MJO phase and dM is the average length (in days) of the MJO phase. The uncertainty in the Z_{250}-center location is estimated through bootstrapping. Each time the Z_{250}-center location is estimated from a subsample (1/8 of the total MJO days for a particular phase) mean and this is repeated 2000

499 times. These statistical analyses have been applied to each model (Supplementary Figs. 9-19).

500

501 **Metrics**

502 The MJO-induced variability is defined as the standard deviation of the MJO-phase-composited
503 anomaly across the eight MJO phases. The eastward extension of the MJO itself is measured by
504 the eastward shift in the longitudinal centroid (θ_ω) of the tropical MJO ω_{500} variability ($\widehat{\omega}_{500}$).
505 θ_ω is defined as

$$\theta_\omega = \frac{\int_{60^o}^{210^o}\int_{12^oS}^{8^oN} \widehat{\omega}_{500}{}^{+}\, d\phi\, \theta d\theta}{\int_{60^o}^{210^o}\int_{12^oS}^{8^oN} \widehat{\omega}_{500}{}^{+}\, d\phi\, d\theta},$$

506 where ϕ is the latitude and θ is the longitude. $\widehat{\omega}_{500}{}^{+}$ refers to $\widehat{\omega}_{500}$ that is larger than the tropical
507 (12°S to 8°N) mean $\widehat{\omega}_{500}$. Smaller $\widehat{\omega}_{500}$ is omitted in the computation to emphasize the MJO
508 active region.

509

510 The eastward extension of the MJO teleconnection is measured by the eastward shift in the
511 longitudinal centroid ($\theta_{\hat{Z}}$) of the MJO-induced Z_{250} variability ($\hat{Z}_{250}$) in the midlatitudes. $\theta_{\hat{Z}}$ is
512 defined as

$$\theta_{\hat{Z}} = \frac{\int_{130^o}^{230^o}\int_{30^oN}^{50^oN} \hat{Z}_{250}{}^{+}\, d\phi\, \theta d\theta}{\int_{130^o}^{230^o}\int_{30^oN}^{50^oN} \hat{Z}_{250}{}^{+}\, d\phi\, d\theta}.$$

513 $\hat{Z}_{250}{}^{+}$ refers to $\hat{Z}_{250}$ that is larger than three times of the midlatitude (30°N to 50°N) mean $\hat{Z}_{250}$.
514 Smaller $\hat{Z}_{250}$ is omitted in the computation to emphasize the center of the MJO teleconnection
515 pattern.

516

517 The eastward shift of the stationary eddy pattern is measured by the eastward shift in the node of

518 Z^*_{250}, defined as the zero-crossing point of the mean Z^*_{250} averaged from 40°N to 50°N. The
519 longitude of the subtropical jet exit is defined as where the mean jet speed (averaged over 27°N-
520 45°N where the jet peaks) falls below 40 m s^{-1}. The enhanced warming east of the climatological
521 warming pool is measured by the longitudinal gradient in the equatorial (5°S to 5°N) surface
522 warming from 130° to 190°.
523
524 The amplitude of the MJO extratropical teleconnection is measured as the average of the Z_{250}
525 peak values associated with Phase 3 and 7. We choose not to include phase 1 and 5 because in
526 some GCMs their teleconnection patterns do not present a clear Z_{250} peak over the North Pacific.
527 The amplitude of tropical MJO circulation is measured as the area mean (12°S to 8°N, 60° to
528 210°) of the MJO ω_{500} variability.
529

530 **Data availability**

531 The AMIP and CMIP outputs used in this study can be obtained from the CMIP5 and CMIP6
532 archives at https://esgf-node.llnl.gov/projects/esgf-llnl/. The NOAA interpolated outgoing
533 longwave radiation dataset is available at https://psl.noaa.gov/data/gridded/data.interp_OLR.html.
534 The NCEP-DOE reanalysis dataset is publicly available at
535 https://psl.noaa.gov/data/gridded/data.ncep.reanalysis2.html. The ECMWF-ERA5 reanalysis
536 dataset is available at https://www.ecmwf.int/en/forecasts/datasets/reanalysis-datasets/era5.
537

538 **Code availability**

The code for MJO-related analyses and the scripts for preparing MJO heating and mean state (for LBM) are available at https://github.com/wenyuz/MJO_scripts (doi:10.5281/zenodo.3746868). The LBM code can be requested from this site: https://ccsr.aori.u-tokyo.ac.jp/~lbm/sub/lbm.html.

References

51. Taylor, K. E., Stouffer, R. J. & Meehl, G. A. An Overview of CMIP5 and the Experiment Design. *Bull. Amer. Meteor. Soc.* **93**, 485–498 (2011).
52. Eyring, V. *et al.* Overview of the Coupled Model Intercomparison Project Phase 6 (CMIP6) experimental design and organization. *Geoscientific Model Development* **9**, 1937–1958 (2016).
53. Kanamitsu, M. *et al.* NCEP–DOE AMIP-II Reanalysis (R-2). *Bull. Amer. Meteor. Soc.* **83**, 1631–1644 (2002).
54. Copernicus Climate Change Service (C3S). ERA5: Fifth generation of ECMWF atmospheric reanalyses of the global climate . (2017) doi:https://doi.org/10.5065/D6X34W69.
55. Watanabe, M. & Kimoto, M. Atmosphere-ocean thermal coupling in the North Atlantic: A positive feedback. *Quarterly Journal of the Royal Meteorological Society* **126**, 3343–3369 (2000).
56. Watanabe, M. & Jin, F.-F. A Moist Linear Baroclinic Model: Coupled Dynamical–Convective Response to El Niño. *J. Climate* **16**, 1121–1139 (2003).
57. Lee, H.-J. & Seo, K.-H. Impact of the Madden-Julian oscillation on Antarctic sea ice and its dynamical mechanism. *Scientific Reports* **9**, 1–10 (2019).

58. Shao, X., Li, S., Liu, N. & Song, J. The Madden–Julian oscillation during the 2016 summer and its possible impact on rainfall in China. *International Journal of Climatology* **38**, 2575–2589 (2018).
59. CLIVAR-MJO Working Group. MJO Simulation Diagnostics. *J. Climate* **22**, 3006–3030 (2009).
60. Wheeler, M. C. & Hendon, H. H. An All-Season Real-Time Multivariate MJO Index: Development of an Index for Monitoring and Prediction. *Mon. Wea. Rev.* **132**, 1917–1932 (2004).
61. Wenyu Zhou. Code for MJO-related analyses and preparing input for LBM simulations. (Zenodo, 2020). doi:10.5281/zenodo.3746868.

Acknowledgements

This work is supported by Laboratory Directed Research and Development (LDRD) funding from Berkeley Lab, provided by the Director, Office of Science, of the U.S. Department of Energy under contract DE-AC02-05CH11231, and by the National Science Foundation (AGS 1637450). We thank Masahiro Watanabe and Michiya Hayashi for providing the Linear Baroclinic Model.

Author contributions

W.Z. designed the research, ran the simulations and conducted the analysis. All authors contributed to improving the analysis and interpretation. J.M. helped with the setup of the LBM. W.Z. wrote the first draft and all authors edited the paper.

Competing interests

The authors declare no competing interests.

Corresponding author

Correspondence to Wenyu Zhou.

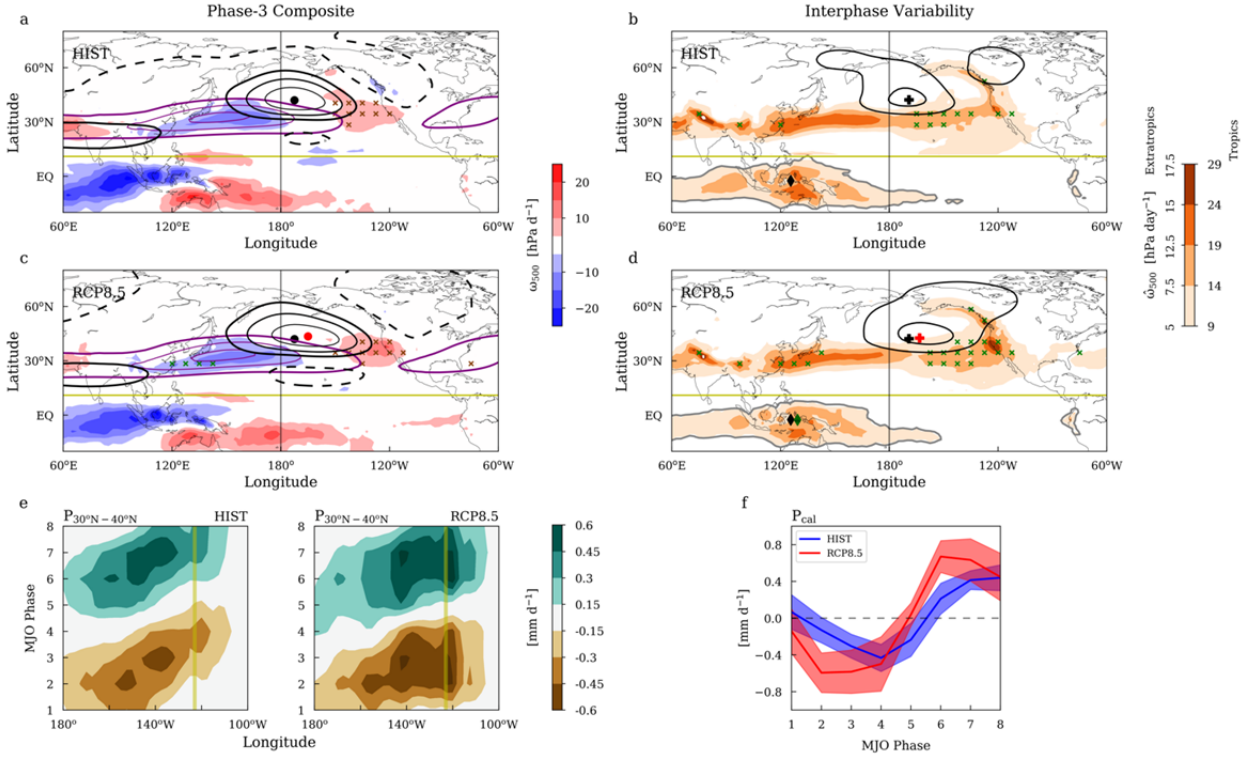

Figure 1: Eastward-extended teleconnection pattern leads to amplified MJO impacts in the Pacific-North America region. a,c, Anomalous Z_{250} (contours at a 12-m interval, solid for positive), ω_{500} (shading) and precipitation (cross symbols where magnitude is larger than 0.35 mm d^{-1}, green for positive) associated with MJO Phase 3 in HIST (**a**) and RCP8.5 (**c**). The subtropical jet, indicated by 250-hPa zonal wind ($\overline{U}_{250}$), is shown as purple contours (levels at 35, 50, 65 m s^{-1}). The dot symbol denotes the Z_{250} center (black for HIST and red for RCP8.5). **b,d,** MJO-induced variability in Z_{250} ($\hat{Z}_{250}$, contours at

levels of 20 and 30 m), ω_{500} ($\widehat{\omega}_{500}$, shading) and precipitation (cross symbols where magnitude is larger than 0.4 mm d^{-1}). The plus symbol denotes the midlatitude $\hat{Z}_{250}$ centroid. The grey contour indicates the boundary of the active MJO region where $\widehat{\omega}_{500}$ exceeds 9 hPa d^{-1}. The diamond symbol denotes the tropical $\widetilde{\omega}_{500}$ centroid (black for HIST and green for RCP8.5). **e,** Precipitation anomaly averaged over 30°N−40°N in HIST and RCP8.5 as a function of the MJO phase and longitude. The yellow line indicates the longitude of California. **f,** Precipitation anomaly averaged over California as a function of the MJO phase in HIST (blue) and RCP8.5 (red). The shading indicates the intermodel standard deviation.

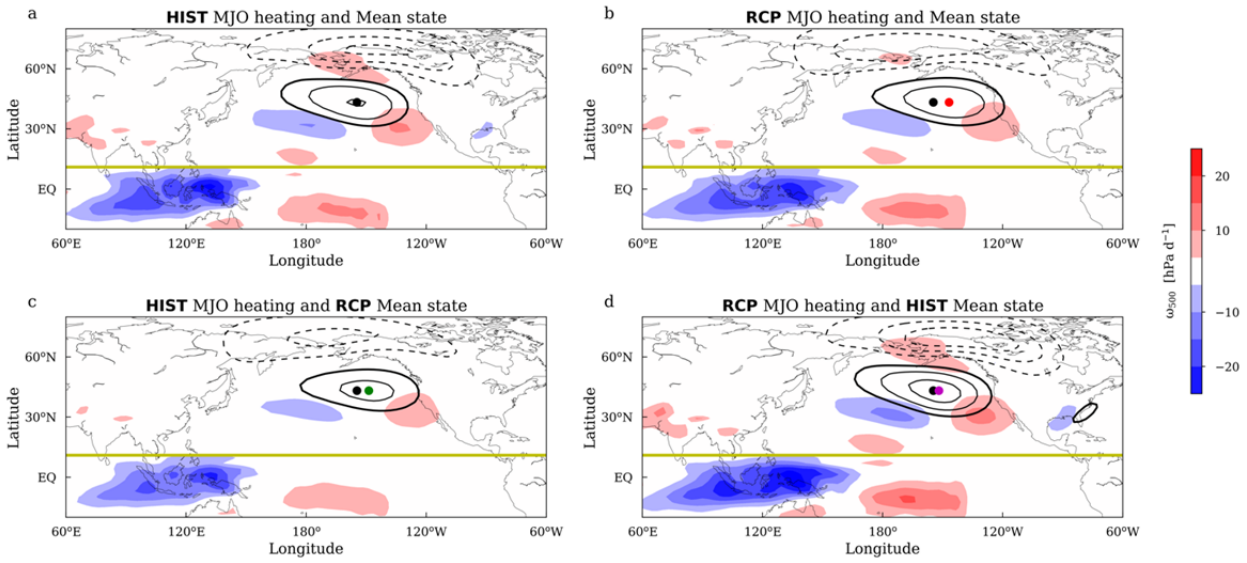

Figure 2: Responses of the MJO teleconnection to changes in MJO heating and large-scale mean state. a, Anomalous Z_{250} (contours at a 12-m interval, solid for positive) and ω_{500} (shading) associated with MJO Phase 3 in LBM. Both MJO heating and mean state are from HIST. **b,** Same as **a** but with MJO heating and mean state both from RCP8.5. **c**, Same as **a** but with mean state from RCP8.5. **d,** Same as **a** but with MJO heating from RCP8.5. The dot symbol denotes the Z_{250} center (black for **a** and colors for **b-d**).

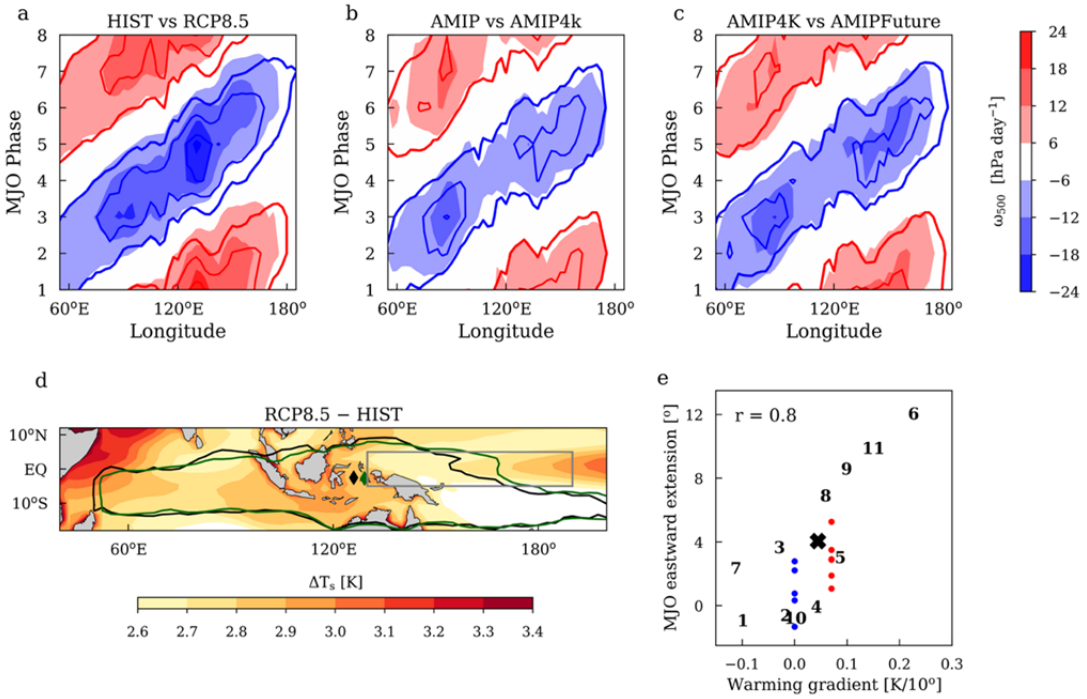

612

613 **Figure 3: Eastward extension of the MJO itself. a,** Anomalous ω_{500} averaged over 10°S-10°N as a
614 function of the MJO phase and longitude in HIST (shading) and RCP8.5 (contours, with the same interval
615 as in HIST). **b,** Same as **a** but for AMIP (shading) and AMIP4K (contours). **c,** Same as **a** but for AMIP4K
616 (shading) and AMIPFuture (contours). **d,** Surface warming pattern projected under anthropogenic
617 warming by the multi-model mean. Boundary (contour) and centroid (diamond symbol) of the active
618 MJO region are denoted (black for HIST and green for RCP8.5). **e,** Intermodel scatterplot between the
619 warming gradient (over the longitudes denoted by the grey box in **d**) and the eastward MJO extension.
620 Individual models are indexed and the cross symbol indicates the multi-model mean. Pearson correlation
621 coefficient r is 0.8. The blue and red dots denote the MJO extension in individual simulations of AMIP4K
622 and AMIPFuture, respectively.

623

624

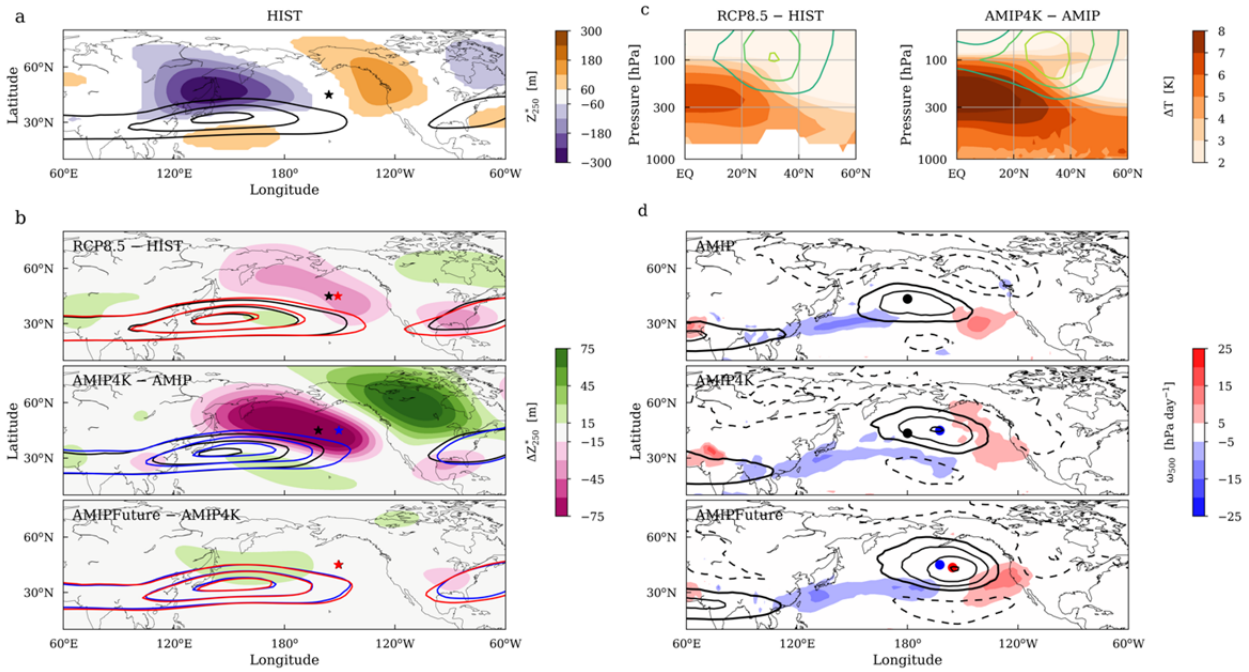

Figure 4: Eastward shift of the subtropical jet exit. a, Z^*_{250} (shading) and $\overline{U}_{250}$ (contour at 35, 45, 55 m s^{-1}) in HIST boreal winter. The star symbol denotes the node of Z^*_{250}. **b,** Responses of Z^*_{250} (changes in shading and nodes denoted by star symbols) and $\overline{U}_{250}$ (contours) to anthropogenic warming in coupled models (top, from HIST in black to RCP8.5 in red), to uniform warming (middle, from AMIP in black to AMIP4K in blue), and warming pattern (bottom, from AMIP4K in blue to AMIPFuture in red). **c,** Changes in the zonal-mean temperature (shading) and zonal wind (contours; 2.5 m s^{-1} interval) under anthropogenic warming (left, from HIST to RCP8.5) and forced by uniform surface warming (right, from AMIP to AMIP4K). **d,** MJO Phase-3 teleconnection in simulations of AMIP, AMIP4K, and AMIPFuture. The dot symbol denotes the Z_{250} center (black for AMIP, blue for AMIP4K and red for AMIPFuture).

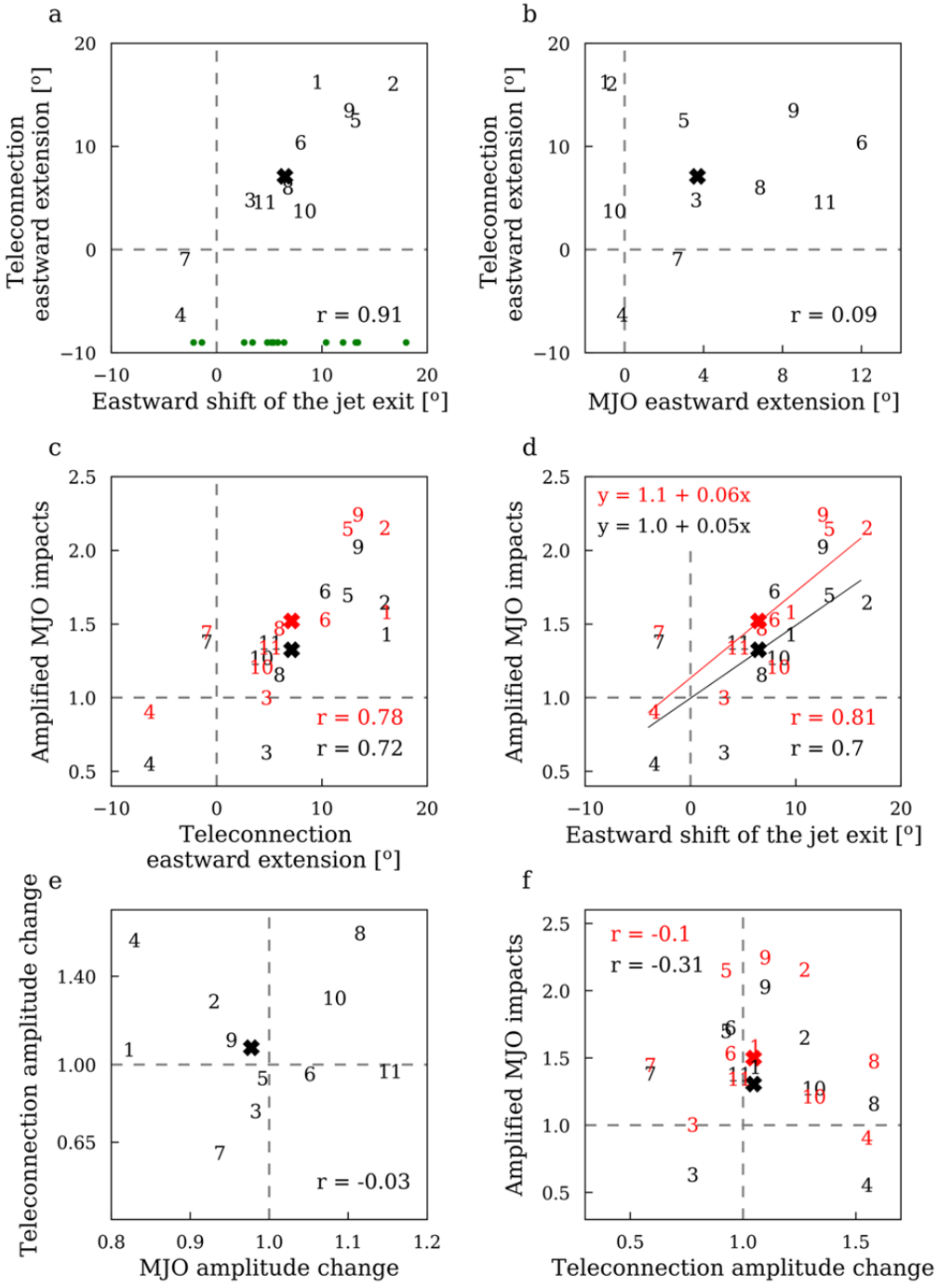

637

638 **Figure 5: Intermodel scatterplots. a,** Eastward shift of the jet exit vs. eastward extension of the MJO
639 teleconnection. The eleven selected models are indexed while the fourteen models not selected are
640 denoted by green dots. The cross symbol indicates the eleven-model mean. **b,** Eastward extension of the
641 MJO itself vs. eastward extension of the MJO teleconnection. **c,** Eastward extension of the MJO

642 teleconnection vs. amplified MJO impacts in California (black for ω_{500}; red for precipitation). **d,**
643 Eastward shift of the jet exit vs. amplified MJO impacts in California (black for ω_{500}; red for
644 precipitation). **e,** MJO amplitude change vs. teleconnection amplitude change. **f,** Teleconnection
645 amplitude change vs. amplified MJO impacts in California (black for ω_{500}; red for precipitation). Pearson
646 correlation coefficients r are shown. Correlation is significant at p-value of 0.05 if $r > 0.58$.

a

Phase-3 Composite

HIST

60°N
30°N
EQ
Latitude

60°E
120°E
180°
120°W
60°W
Longitude

b

Interphase Variability

HIST

60°N
30°N
EQ
Latitude

60°E
120°E
180°
120°W
60°W
Longitude

ω_{500} [hPa d^{-1}]

20
10
−10
−20

c

RCP8.5

60°N
30°N
EQ
Latitude

60°E
120°E
180°
120°W
60°W
Longitude

d

RCP8.5

60°N
30°N
EQ
Latitude

60°E
120°E
180°
120°W
60°W
Longitude

$\hat{\omega}_{500}$ [hPa day^{-1}]

Extratropics
17.5
15
12.5
7.5
5

Tropics
29
24
19
14
9

e

$P_{30°N-40°N}$ HIST

$P_{30°N-40°N}$ RCP8.5

MJO Phase
8
7
6
5
4
3
2
1

180°
140°W
100°W
Longitude

[mm d^{-1}]

0.6
0.45
0.3
0.15
-0.15
-0.3
-0.45
-0.6

f

P_{cal}

HIST
RCP8.5

[mm d^{-1}]
0.8
0.4
0.0
−0.4
−0.8

1
2
3
4
5
6
7
8
MJO Phase

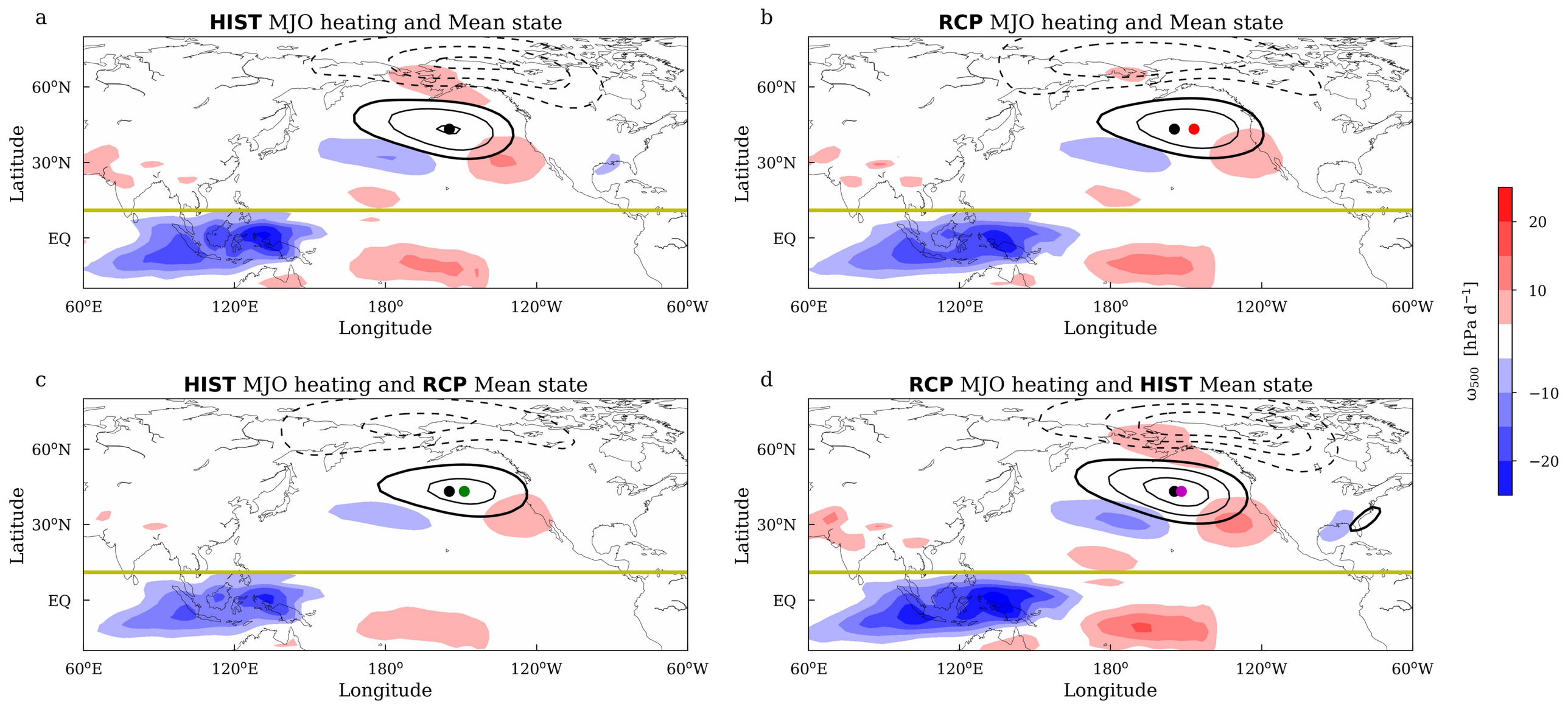
a
HIST MJO heating and Mean state
b
RCP MJO heating and Mean state
c
HIST MJO heating and RCP Mean state
d
RCP MJO heating and HIST Mean state
60°N
30°N
EQ
Latitude
60°E
120°E
180°
120°W
60°W
Longitude
20
10
−10
−20
ω500 [hPa d−1]

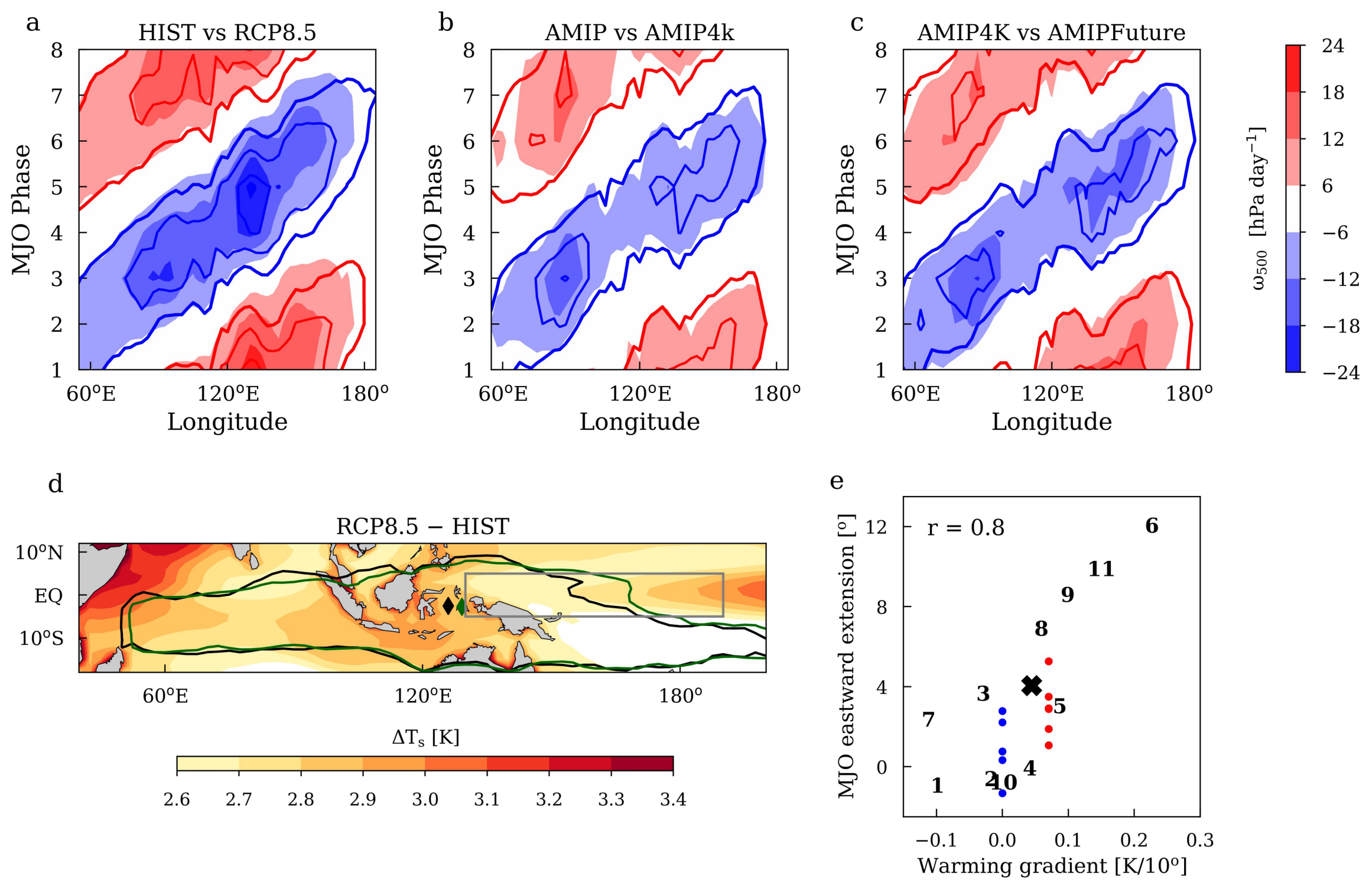
a
HIST vs RCP8.5
b
AMIP vs AMIP4k
c
AMIP4K vs AMIPFuture
MJO Phase
Longitude
60°E
120°E
180°
ω_{500} [hPa day^{-1}]
24
18
12
6
−6
−12
−18
−24
d
RCP8.5 − HIST
10°N
EQ
10°S
ΔT_s [K]
2.6
2.7
2.8
2.9
3.0
3.1
3.2
3.3
3.4
e
r = 0.8
MJO eastward extension [°]
Warming gradient [K/10°]
−0.1
0.0
0.1
0.2
0.3
0
4
8
12
1
2
3
4
5
6
7
8
9
10
11

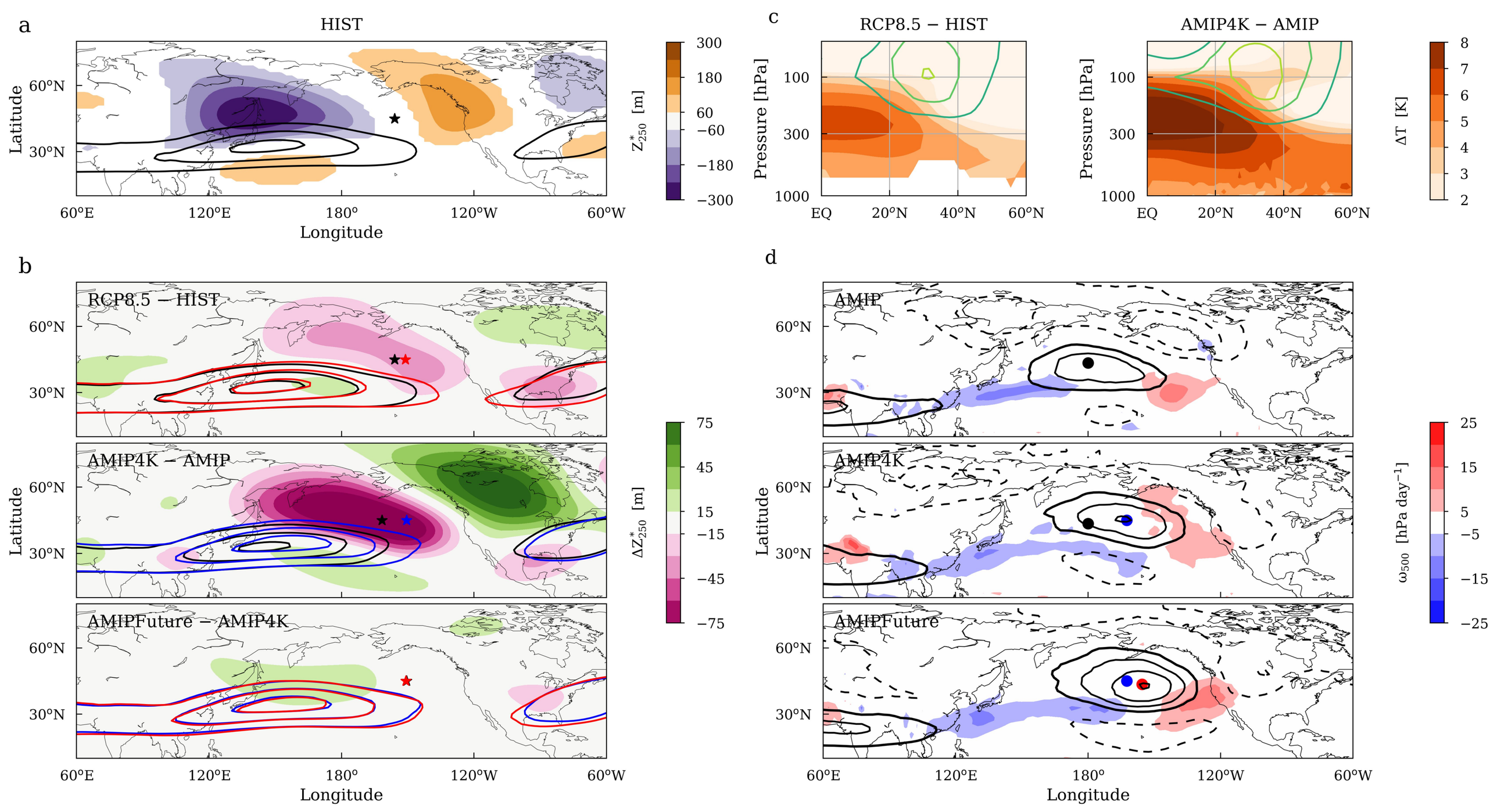
a
HIST
Latitude
60°N
30°N
60°E
120°E
180°
120°W
60°W
Longitude
300
180
60
−60
−180
−300
Z^*_{250} [m]
c
RCP8.5 − HIST
AMIP4K − AMIP
Pressure [hPa]
100
300
1000
EQ
20°N
40°N
60°N
8
7
6
5
4
3
2
ΔT [K]
b
RCP8.5 − HIST
AMIP4K − AMIP
AMIPFuture − AMIP4K
75
45
15
−15
−45
−75
ΔZ^*_{250} [m]
d
AMIP
AMIP4K
AMIPFuture
25
15
5
−5
−15
−25
ω_{500} [hPa day^{-1}]

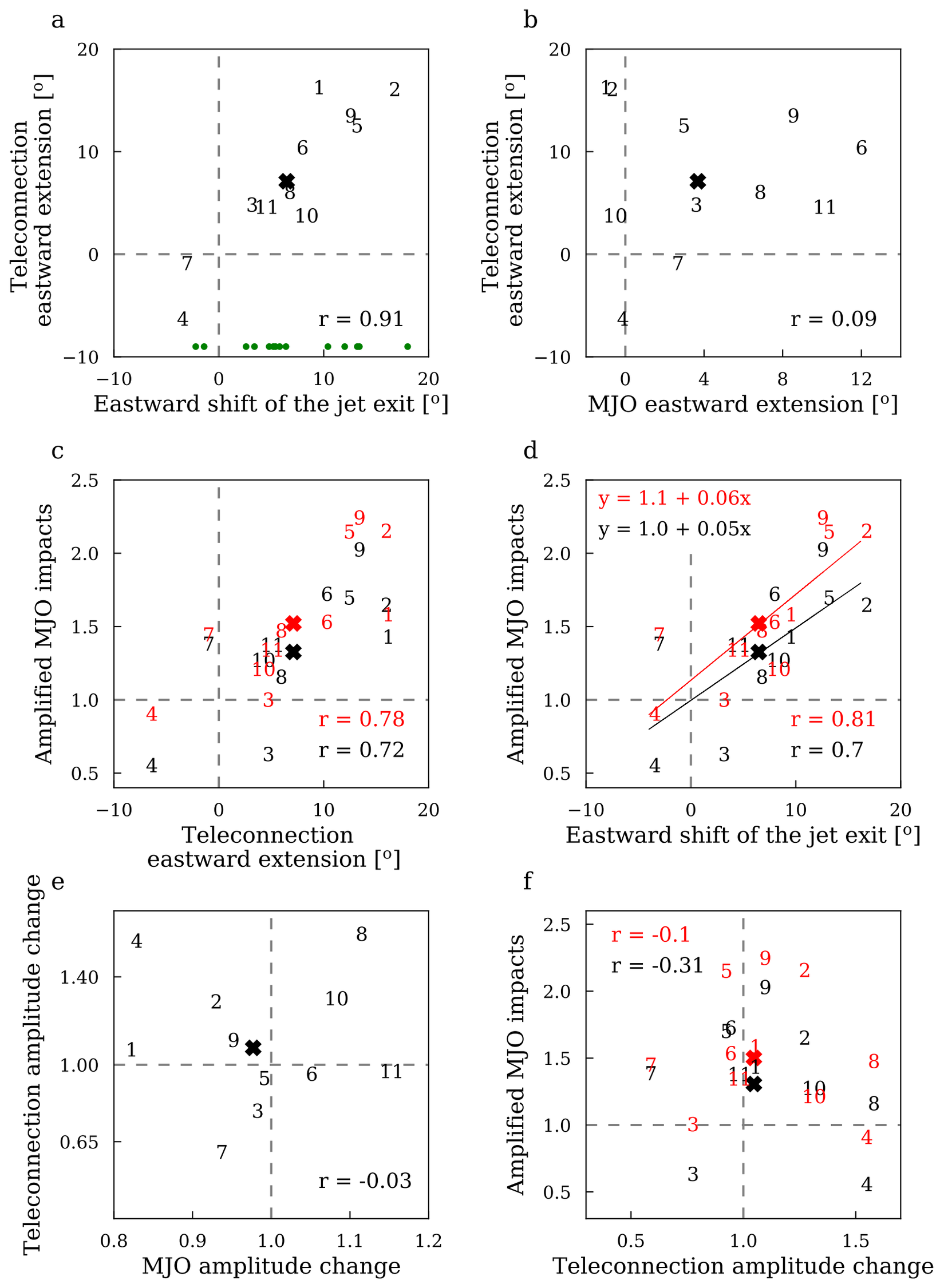
a
Teleconnection eastward extension [°]
Eastward shift of the jet exit [°]
r = 0.91
b
Teleconnection eastward extension [°]
MJO eastward extension [°]
r = 0.09
c
Amplified MJO impacts
Teleconnection eastward extension [°]
r = 0.78
r = 0.72
d
y = 1.1 + 0.06x
y = 1.0 + 0.05x
Amplified MJO impacts
Eastward shift of the jet exit [°]
r = 0.81
r = 0.7
e
Teleconnection amplitude change
MJO amplitude change
r = -0.03
f
r = -0.1
r = -0.31
Amplified MJO impacts
Teleconnection amplitude change